

# Learning Ordinality in Semantic Segmentation

Rafael Cristino<sup>1</sup>      Ricardo P. M. Cruz<sup>1,2\*</sup>  
Jaime S. Cardoso<sup>1,2\*</sup>

<sup>1</sup> Faculty of Engineering, University of Porto

<sup>2</sup> INESC TEC, Porto

\* rrcruz@fe.up.pt, jaime.cardoso@fe.up.pt

July 31, 2024

## Abstract

Semantic segmentation consists of predicting a semantic label for each image pixel. Conventional deep learning models do not take advantage of ordinal relations that might exist in the domain at hand. For example, it is known that the pupil is inside the iris, and the lane markings are inside the road. Such domain knowledge can be employed as constraints to make the model more robust. The current literature on this topic has explored pixel-wise ordinal segmentation methods, which treat each pixel as an independent observation and promote ordinality in its representation. This paper proposes novel spatial ordinal segmentation methods, which take advantage of the structured image space by considering each pixel as an observation dependent on its neighborhood context to also promote ordinal spatial consistency. When evaluated with five biomedical datasets and multiple configurations of autonomous driving datasets, ordinal methods resulted in more ordinally-consistent models, with substantial improvements in ordinal metrics and some increase in the Dice coefficient. It was also shown that the incorporation of ordinal consistency results in models with better generalization abilities.

## 1 Introduction

Semantic segmentation, or scene parsing, is the task of attributing a semantic label to each of the pixels in an image, resulting in a segmentation map. One common problem with these deep learning segmentation models is the lack of generalization ability, which means that the network fails to make appropriate predictions when parsing a situation that did not occur in the training dataset [1]. A hypothesis is that the neural network model does not have the necessary intrinsic domain knowledge of the task – it failed to infer appropriate high-level relations from the data used to train it.

In many situations, there is an explicit ordering between the output classes, and by training the network with methods that uphold the ordinal constraints, the network may be able to learn better higher-level concepts, such as the ordinal relation between different objects (e.g., the lane marks and are inside the lane,

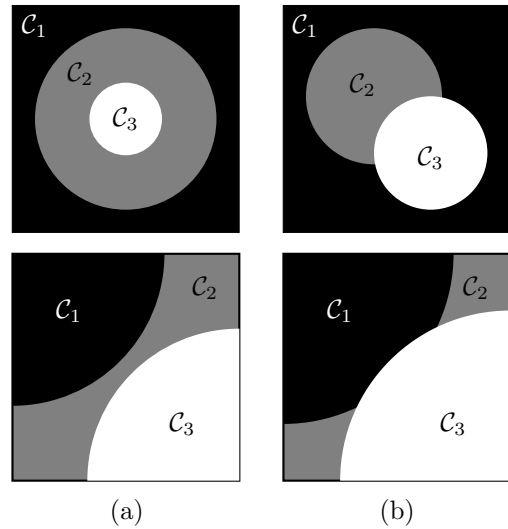


Figure 1: Example of (a) segmentation masks and (b) hypothetical non-constrained model outputs for an ordinal problem with three distinct classes,  $\{C_1, C_2, C_3\}$ , where such an order is defined that  $C_1 \supset C_2 \supset C_3$ , therefore, an area segmented as  $C_1$  can only possibly have a direct boundary with areas segmented as  $C_2$ , whereas  $C_2$  can have boundaries both with  $C_1$  and  $C_3$ .

etc) and the relative placement of objects (e.g., the sidewalk is to the side of the road, etc.).

Typically, ordinal problems have mostly been studied in the context of (image) classification [2–4], where the task is to classify an observation (image) as one of  $C_1 < C_2 < \dots < C_K$  ordered classes (for example, the severity of a disease), as opposed to nominal classes in the case of classic nominal classification. To our knowledge, only one work [5] attempted to introduce such ordinal relations for semantic segmentation, where  $C_1 \supset C_2 \supset \dots \supset C_K$ . However, the work does not explicitly perform spatial segmentation: it would be expected that an area labelled as  $C_k$  would only have a direct boundary to the areas segmented as  $C_{k-1}$  and  $C_{k+1}$ , as exemplified in Figure 1.

The transition from image classification to segmentation inherently evolves the prediction task from classifying independent samples (each image) to classifying structured dependent samples (each pixel in an image). The former can only take action in the repre-

sentation space of each pixel, while the latter can also consider the structured space and the relations between the samples. Further developing this idea, the structured image space can be generalized to a graph, where each pixel is a vertex and is connected to its adjacent pixels.

The contributions presented in this paper can be summarized in:

- The task of ordinal regression is formalized into ordinal consistency for each individual decision and ordinal consistency for the entire structure of the input, i.e. spatial consistency in the case of images (section 3.1).
- Focusing on the latter case, two loss regularization terms (section 3.3) and one metric are proposed (section 3.5).
- A thorough evaluation is performed for five biomedical datasets and an autonomous driving dataset.

The document is structured as follows: Section 2 introduces the state of the art; Section 3 delineates the proposal; Section 4 describes the conducted experiments; Section 5 shows and analyzes the experimental results; and Section 6 revisits the proposed methods and summarizes the key conclusions.

## 2 State of the Art

Cross entropy is one of the most commonly used loss functions for image classification and segmentation problems. Defining cross entropy for a semantic segmentation problem,

$$\text{CE}(\mathbf{y}_n, \hat{\mathbf{p}}_n) = -\frac{1}{HW} \sum_{i=1}^H \sum_{j=1}^W \sum_{k=1}^K \mathbb{1}(y_{n,i,j} = k) \log(\hat{p}_{n,k,i,j}) \quad (1)$$

where  $\hat{\mathbf{p}}$  is the model output as probabilities, in shape  $(N, K, H, W)$ , where  $N$  is the batch size,  $K$  is the number of classes, and  $(H, W)$  are, respectively, the height and width of each image;  $\mathbf{y}$  is the ground truth segmentation map, in shape  $(N, H, W)$ , where each value  $y_{n,i,j}$  corresponds to the ground truth class  $k \in \{1, \dots, K\}$  of the pixel at position  $(i, j)$  of observation  $n$ ; and  $\mathbb{1}(x)$  is the indicator function of  $x$ .

Cross-entropy maximizes the probability of the ground truth class for each pixel in the observation, ignoring the distribution of the predictions for the other classes. This is a potential area where new loss functions can improve by restricting the probabilities of the non-ground truth class according to the domain knowledge of the task.

### 2.1 Ordinal Classification Methods

Various research works seek to imbue deep neural networks with ordinal domain knowledge in the ordinal classification domain.

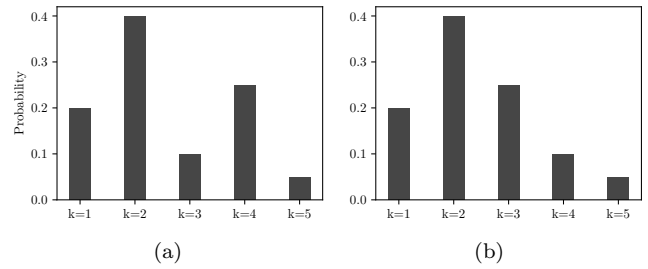


Figure 2: Example of possible (a) multimodal and (b) unimodal output probability distributions for a given pixel.

#### 2.1.1 Unimodality

The promotion of unimodality in the distribution of the model output probabilities has achieved good results in ordinal classification tasks [3, 6–8]. This can be advantageous in ordinal problems because the model should be more uncertain between ordinally adjacent classes. For example, it would not make sense for a model to output a high probability for Low and High risk of disease, but a small probability for Medium risk of disease. Figure 2 shows the difference between multimodal and unimodal distributions.

To promote unimodal output probability distributions, some authors have imposed architectural restrictions, which restrict the network output to a Binomial or Poisson probability distributions [6, 7]. Other authors have promoted ordinality by penalizing the model when it outputs a non-unimodal distribution through augmented loss functions. One such case is the CO2 loss, which penalizes neighbor class probabilities if they do not follow unimodal consistency [3],

$$L_{\text{CO2}}(y_n, \hat{\mathbf{p}}_n) = L_{\text{CE}}(y_n, \hat{\mathbf{p}}_n) + \lambda L_{\text{O2}}(y_n, \hat{\mathbf{p}}_n), \quad (2)$$

$$L_{\text{O2}}(y_n, \hat{\mathbf{p}}_n) = \sum_{k=1}^{K-1} \mathbb{1}(k \geq y_n) \text{ReLU}(\delta + \hat{p}_{n,k+1} - \hat{p}_{n,k}) + \sum_{k=1}^{K-1} \mathbb{1}(k \leq y_n) \text{ReLU}(\delta + \hat{p}_{n,k} - \hat{p}_{n,k+1}), \quad (3)$$

with  $\delta$  being an imposed margin, assuring that the difference between consecutive probabilities is at least  $\delta$ , and ReLU is defined as  $\text{ReLU}(x) = \max(0, x)$ .

#### 2.1.2 Ordinal Encoding

An approach to introducing ordinality to neural networks for classification involves regularizing the input data by encoding the ordinal distribution in the ground truth labels [9]. Defining  $k^*$  as the ground truth class for a given sample, this input data encoding encodes each class as  $\mathbb{1}(k < k^*)$ , whereas generic one-hot encoding encodes each class as  $\mathbb{1}(k = k^*)$ . This approach can be adapted for segmentation problems by similarly encoding the ground truth masks at a pixel level [5].

Using ordinal encoding for segmentation does not guarantee that the output probabilities are monotonous, i.e., the probability of ordinal class  $k$ ,  $P_k$ , may be less than  $P_{k+1}$ . The consistency of the output class probabilities can be achieved by using,

$$P(\mathcal{C}_{k+1}^+) = P(\mathcal{C}_{k+1}^+ | \mathcal{C}_k^+)P(\mathcal{C}_k^+), \quad (4)$$

where  $P(\mathcal{C}_{k+1}^+ | \mathcal{C}_k^+)$  is the  $(k + 1)$ -th output of the network and  $P(\mathcal{C}_k^+)$  is the corrected probability of class  $k$  [5].

The state-of-the-art ordinal segmentation approaches have treated pixels as independent observations and promoted ordinality in their representation. However, this may be insufficient when applied to the structured image space, where pixels are dependent observations and a new level of consistency, i.e., spatial consistency, can be achieved.

### 3 Proposal

Firstly, we present the formal foundation of our work (Section 3.1), then introduce the proposed ordinal segmentation methods, which are categorized into representation consistency (Section 3.2), and structural consistency (Section 3.3). Finally, the ordinal segmentation problem is adapted to domains with arbitrary hierarchies (Section 3.4).

#### 3.1 Foundation

We start by recovering the definition of ordinal models, as introduced in [10, 11]. In a model consistent with the ordinal setting, a small change in the input data should not lead to a “big jump” in the output decision. Assuming  $f(\mathbf{x})$  as a decision rule that assigns each input value  $\mathbf{x} \in \mathbb{R}^d$  to the index  $\in \{1, 2, \dots, K\}$  of the predicted class, the decision rule is said to be consistent with an ordinal data classification setting in a point  $\mathbf{x}_0$  only if

$$\exists \varepsilon > 0, \quad \max_{\mathbf{x} \in \mathcal{B}_\varepsilon(\mathbf{x}_0)} f(\mathbf{x}) - \min_{\mathbf{x} \in \mathcal{B}_\varepsilon(\mathbf{x}_0)} f(\mathbf{x}) \leq 1,$$

with  $\mathcal{B}_\varepsilon$  representing the individual feature-space neighborhood centered in  $\mathbf{x}_0$  with radius  $\varepsilon$ . Equivalently, the decision boundaries in the input feature-space  $\mathbf{x}$  should be only between regions of consecutive classes. Note that the concept of consistency with the ordinal setting is independent of the model type (probabilistic or not) and relies only on the decision region produced by the model. The state-of-the-art methods discussed in the previous Section focus only on this consistency (albeit often indirectly, by working on a related property, like the unimodality in the output probability space).

However, this consistency is only part of our knowledge in the ordinal segmentation setting. In Figure 3, the feature description  $\mathbf{x} \in \mathbb{R}$  at every pixel is mapped

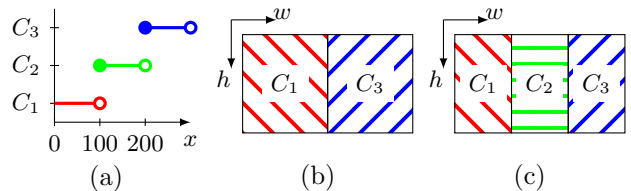


Figure 3: Illustration of possible ordinal (in)consistencies. (a) Ordinal representation consistency. (b) Ordinal structure inconsistency. (c) Ordinal structure consistency.

to the class according to the representation function

$$f(x) = \begin{cases} \mathcal{C}_1, & \text{if } x < 100 \\ \mathcal{C}_2, & \text{if } 100 \leq x < 200 \\ \mathcal{C}_3, & \text{if } x \geq 200, \end{cases} \quad (5)$$

which is also depicted in Figure 3(a). Note that the model is ordinal-consistent in the pixel description space. At most, a small change in  $x$  will change the decision to an adjacent class.

Consider now that the representation learned at each pixel  $v$  is given as

$$\mathbf{x}(v) = \begin{cases} \mathbf{x}(v_0), & \text{if } v \in \text{left half of the image} \\ 4\mathbf{x}(v_0), & \text{if otherwise,} \end{cases} \quad (6)$$

where  $\mathbf{x}(v_0)$  is arbitrarily defined. The model always sets the right half of the image to four times the values in the left half. Therefore, as illustrated in Figure 3(b), even being consistent at the pixel representation level, for some images (e.g., when the description of the pixels on the left takes the value 75), the decision will be  $\mathcal{C}_1$  for the left half and  $\mathcal{C}_3$  for the right half, which is to be avoided in an ordinal segmentation scenario. Therefore, we generalize the definition of ordinal-consistent models to models acting on structured observations, such as images or, more generally, graphs.

Consider each image as a graph  $\mathcal{G} = (\mathcal{V}, \mathcal{E})$ , where  $\mathcal{V}$  denotes the set of graph vertices and  $\mathcal{E} \subset \mathcal{V} \times \mathcal{V}$  denotes the set of graph edges. Vertices in the image graph represent pixels, and because the values of a pixel are usually highly related to the values of its neighbors, there are undirected edges from a pixel to its neighboring pixels (often 4 or 8). The corresponding graph is then a 2D lattice. Consider the goal of learning a function of signals/features which takes as input:

- A feature description  $\mathbf{x}_i = g(v_i)$  for every node  $v_i$
- A representative description of the graph structure  $\mathcal{G} = (\mathcal{V}, \mathcal{E})$

and produces a node-level output  $f(\mathbf{x}_i)$ . Also, remember that the closed neighborhood of a vertex  $v$  in a graph  $\mathcal{G}$  is the subgraph of  $\mathcal{G}$ ,  $\mathcal{N}[v]$ , induced by all vertices adjacent to  $v$  and  $v$  itself, i.e., the graph composed of the vertices adjacent to  $v$  and  $v$ , and all edges connecting vertices adjacent to  $v$ .

We now define a model as ordinal consistent if the following two conditions are simultaneously met:

- **representation consistency:** as before, if, for every point  $\mathbf{x}_0 \in \mathbb{R}^d$ ,  $\exists \varepsilon > 0$ ,  $\max_{\mathbf{x} \in \mathcal{B}_\varepsilon(\mathbf{x}_0)} f(\mathbf{x}) - \min_{\mathbf{x} \in \mathcal{B}_\varepsilon(\mathbf{x}_0)} f(\mathbf{x}) \leq 1$ , with  $\mathcal{B}_\varepsilon$  representing the feature-space neighborhood centered in  $\mathbf{x}_0$  with radius  $\varepsilon$ .
- **structural consistency:** if, for every node  $v_i$ ,  $\max_{v \in \mathcal{N}[v_i]} f(g(v)) - \min_{v \in \mathcal{N}[v_i]} f(g(v)) \leq 1$

Figure 3(b) illustrates structural inconsistency and consistency – the representations of the pixels change smoothly over the image as given by

$$\mathbf{x}(v) = \begin{cases} \mathbf{x}(v_0), & \text{if } v \in \text{left third of the image} \\ \mathbf{x}(v_0) + 1, & \text{if } v \in \text{middle third of the image} \\ \mathbf{x}(v_0) + 2, & \text{if } v \in \text{right third of the image.} \end{cases} \quad (7)$$

### 3.2 Representation Consistency for Ordinal Segmentation

In ordinal segmentation, ordinal representation consistency methods encompass those methods that act on the individual pixel representation  $\mathbf{x}(v)$  and decision, i.e., they impose restrictions on the pixel, taking into account its own characteristics and disregarding the context of the neighboring pixels. Such methods include the ordinal pixel encoding and consistency methods discussed in the state-of-the-art analysis [5]. The previously introduced CO2 loss (4) can be trivially adapted to segmentation by performing the regularization term for each pixel,

$$L_{O2}(\mathbf{y}_n, \hat{\mathbf{p}}_n) = \frac{1}{HW} \sum_{i=1}^W \sum_{j=1}^H \left[ \sum_{k=1}^{y_{n,i,j}} \text{ReLU}(\delta + \hat{p}_{n,k,i,j} - \hat{p}_{n,k+1,i,j}) + \sum_{k=y_{n,i,j}}^{K-1} \text{ReLU}(\delta + \hat{p}_{n,k+1,i,j} - \hat{p}_{n,k,i,j}) \right]. \quad (8)$$

### 3.3 Structural Consistency for Ordinal Segmentation

The structural neighborhood concerns the neighborhood that relates one element with the others in the graph structure. In the case of semantic segmentation, the structural neighborhood is the set that contains all pixels connected to a given pixel.

#### 3.3.1 Contact Surface Loss Using Neighbor Pixels

The contact surface loss is defined by penalizing the prediction of two neighboring pixels of non-ordinally adjacent classes. This penalization term is performed

by multiplying the output probabilities for neighbouring pixels,

$$L_{CSNP}(\hat{\mathbf{p}}_n, \hat{\mathbf{p}}_m) = \sum_{\substack{n,m: \\ v_n \in \mathcal{N}[v_m]}} \hat{\mathbf{p}}_n^T C \hat{\mathbf{p}}_m \quad (9)$$

where  $\hat{\mathbf{p}}_n^T C \hat{\mathbf{p}}_m$  is a symmetric bilinear form,  $C$  is a  $K \times K$  cost matrix,  $\hat{\mathbf{p}}_n \in \mathbb{R}^K$  is the vector of probabilities predicted at node  $v_n$  (similarly for  $\mathbf{p}_m$ ).  $C$  is defined as

$$C_{i,j} = \text{ReLU}(|i-j|-1) = \begin{cases} 0, & \text{if } |i-j| \leq 1 \\ C_{i,j} = |i-j| - 1, & \text{otherwise,} \end{cases} \quad (10)$$

to penalize ordinal-inconsistent neighboring probabilities, where  $\text{ReLU}(\cdot)$  is the Rectified Linear function,  $\text{ReLU}(x) = \max(0, x)$ . As an example, for  $K = 4$  classes, we obtain

$$C = \begin{bmatrix} 0 & 0 & 1 & 2 \\ 0 & 0 & 0 & 1 \\ 1 & 0 & 0 & 0 \\ 2 & 1 & 0 & 0 \end{bmatrix}.$$

The intuition is to penalize high probabilities in spatially-close classes that are not adjacent.

#### 3.3.2 Contact Surface Loss Using the Distance Transform

Another approach is leveraging the distance transform, which is an image map where each value represents the distance from each pixel in the target image to its closest pixel with value 1, calculated with the customizable distance function  $d$  [12]. Defining the distance transform (DT) of the output probability map of class  $k$ ,

$$\text{DT}(\hat{\mathbf{p}}_{n,k})_{p_1} = \min_{p_2: \hat{p}_{n,k,p_2} \geq \delta} d(p_1, p_2), \quad (11)$$

where  $p = (i, j)$  and  $\delta$  is the threshold parameter that selects the high-confidence pixels (typically 0.5), allowing the distance transform to be calculated for a high-certainty version of the output segmentation mask.

This provides a distance between pixels that have a high probability for a certain class and the closest pixel with a low probability of that class. That is, it provides an approximate distance between pixels of different classes. The model is trained to maximize this distance by multiplying the class probabilities map with the opposing class's distance transform,

$$L_{\text{CSDT}}(\hat{\mathbf{p}}_n) = -\frac{1}{|\mathcal{S}|} \sum_{k_1, k_2 \in \mathcal{S}} C_{k_1, k_2} (\hat{\mathbf{p}}_{n, k_1} \text{DT}(\hat{\mathbf{p}}_{n, k_2}) + \hat{\mathbf{p}}_{n, k_2} \text{DT}(\hat{\mathbf{p}}_{n, k_1})), \quad (12)$$

where  $\mathcal{S}$  is the set of pairs  $(k_1, k_2) \in \{1, \dots, K\}$  such that  $k_2 - k_1 > 1$ .

At this stage, the CSDT term maximizes the distance indefinitely. This is problematic because this may cause exploding distances, drawing the masks

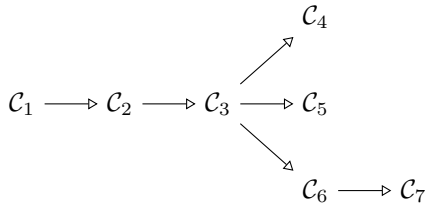


Figure 4: A Hasse diagram exemplifying a domain with a partial order in its set of classes.

away from each other and possibly completely deviating from the ground truth. This can be solved by limiting the distance transform to a maximum distance,  $\gamma$ . This way, the loss only penalizes masks closer to each other than the  $\gamma$  value. For that reason, an updated distance transform was used, which saturates,

$$DT(\hat{\mathbf{p}}_{n,k})_{p_1}^\gamma = \min(DT(\hat{\mathbf{p}}_{n,k})_{p_1}, \gamma). \quad (13)$$

### 3.4 Partially Ordered Domains

The previous ordinal segmentation methods were proposed for ordinal domains with a (linear) total order in the set of classes, i.e., domains where  $\mathcal{C}_1 \supset \mathcal{C}_2 \supset \dots \supset \mathcal{C}_K$ . This section proposes extending the previous work on ordinal losses to partially ordered output sets (e.g., the road may contain both lane marks and vehicles, but there is no relation between lane marks and vehicles).

Domains with a partial order in their set of classes must provide the segmentation methods with this partial order, i.e., the ordinal relations that motivate the ordinal constraints, as exemplified by Figure 4.

The ordinal segmentation metrics and losses proposed to total order sets can be extended to partially ordered sets. Define first  $\ell_{m,n}$  as the length of the shortest path from class  $m$  to class  $n$  in the Hasse diagram, or 0 if no such path exists. Note that  $\ell_{m,n} \neq \ell_{n,m}$  and  $\ell_{m,n} \vee \ell_{n,m} = 0$ .

The previously introduced loss terms ( $L_{O2}$ ,  $L_{CSNP}$  and  $L_{CSDT}$ ) are extended to arbitrary hierarchies as  $L'_{O2}$ ,  $L'_{CSNP}$  and  $L'_{CSDT}$ .

The  $L'_{O2}$  term can be redefined from (8) by applying it between two neighboring classes, i.e. only when  $\ell_{m,n} = 1$ , and if the edge  $(m,n)$  is part of a Hasse path that includes the ground-truth label  $k^*$ .

The  $C$  cost matrix in the  $L'_{CSNP}$  term can be defined as

$$C_{m,n} = \text{ReLU}(\max(\ell_{m,n}, \ell_{n,m}) - 1).$$

The adaptation  $L'_{CSDT}$  is similar to the adopted in  $L'_{O2}$ .

Note that all these extensions revert to the base versions when applied to a totally ordered set.

## 3.5 Evaluation Metrics

### 3.5.1 Unimodal Pixels

We propose measuring the representation consistency using as a metric the percentage of Unimodal Pixels

Table 1: A selection of appropriate biomedical datasets for ordinal segmentation.

Dataset	# Images	# Classes	Sample
Breast Aesthetics [13]	120	4	
Cervix-MobileODT [14]	1480	5	
Mobbio [15]	1817	4	
Teeth-ISBI [16]	40	5	
Teeth-UCV [17]	100	4	

(UP), originally proposed by [8], which consists of the fraction of times that the probability distribution produced by the model is unimodal.

### 3.5.2 Contact Surface Metric

To evaluate the structural consistency, we propose to measure the percentage of ordinally invalid inter-class jumps between adjacent pixels, a metric for the contact surface between the masks of non-ordinally adjacent classes. Ordinally valid jumps are considered to be jumps between classes whose ordinal distance equals 1. If the ordinal distance between the classes of adjacent pixels exceeds 1, then that is an ordinally invalid jump. This requires that each pixel and its immediate neighborhood be examined during calculation. Defining the Contact Surface (CS) metric,

$$\begin{aligned} \text{CS}(\hat{\mathbf{y}}_n) = & \frac{1}{2} \frac{\sum_{i=1}^H \sum_{j=1}^W \mathbb{1}(\text{CS}_{\text{dx}}(\hat{\mathbf{y}}_n)_{i,j} > 1)}{\sum_{i=1}^H \sum_{j=1}^W \mathbb{1}(\text{CS}_{\text{dx}}(\hat{\mathbf{y}}_n)_{i,j} > 0)} \\ & + \frac{1}{2} \frac{\sum_{i=1}^H \sum_{j=1}^W \mathbb{1}(\text{CS}_{\text{dy}}(\hat{\mathbf{y}}_n)_{i,j} > 1)}{\sum_{i=1}^H \sum_{j=1}^W \mathbb{1}(\text{CS}_{\text{dy}}(\hat{\mathbf{y}}_n)_{i,j} > 0)}, \end{aligned} \quad (14)$$

where  $\hat{\mathbf{y}} = \text{argmax}_{k=1}^K(\hat{\mathbf{p}})$ , and  $\text{CS}_{\text{dx}}$  and  $\text{CS}_{\text{dy}}$  are the ordinal index variation, i.e., ordinal distance, from the current pixel  $(i,j)$  to the neighborhood, respectively, through the  $x$  and  $y$  axis,

$$\begin{aligned} \text{CS}_{\text{dx}}(\hat{\mathbf{y}}_n)_{i,j} &= |\hat{\mathbf{y}}_{n,i,j} - \hat{\mathbf{y}}_{n,i,j+1}| \\ \text{CS}_{\text{dy}}(\hat{\mathbf{y}}_n)_{i,j} &= |\hat{\mathbf{y}}_{n,i,j} - \hat{\mathbf{y}}_{n,i+1,j}| \end{aligned} \quad (15)$$

## 4 Experiments

### 4.1 Datasets

Various real-life biomedical datasets with ordinal segmentation tasks, i.e., where there is a clear ordering between classes, were identified from the literature [5]. Table 1 introduces the five biomedical datasets used to validate the proposed methods, along with a sample image and its corresponding segmentation mask.

To evaluate the ordinal methods on autonomous driving domains, the BDD100K [18] and Cityscapes [19] datasets were used:

- BDD100K – is a multi-task, large-scale, and diverse dataset, obtained in a crowd-sourcing manner. Its images are split into two sets, each supporting a different subset of tasks: (1) 100K images – 100,000 images with labels for the object detection, drivable area, and lane marking tasks, and (2) 10K images – 10,000 images with labels for the semantic segmentation, instance segmentation, and panoptic segmentation tasks. The 10K dataset is not a subset of the 100K, but considerable overlap exists.
- Cityscapes – is a large-scale and diverse dataset, with scenes obtained from 50 different cities. It provides 5,000 finely annotated images for semantic segmentation.

Two variants of the BDD100K dataset were considered: (1) BDD10K for the ordinary semantic segmentation task (10,000 images); and (2) BDDIntersected, which is the intersection of the 100K and 10K subsets and supports both the semantic segmentation and drivable area tasks (2,976 images). The models trained with BDD10K were subsequently tested with Cityscapes to validate the methods’ generalization ability with out-of-distribution (OOD) testing. Furthermore, to evaluate how the proposed methods influence learning with scarce data, a dataset scale variation experiment was conducted with the BDD10K dataset.

To transpose semantic segmentation in autonomous driving to an ordinal segmentation problem, ordinal relations must be derived from the classes in the dataset. When analyzing an autonomous driving scene, e.g., Figure 5, we can, a priori, derive that, usually:

- The vehicles will be on the road or in parking spaces;
- The drivable area will be on the road;
- The ego lane will be in the drivable area;
- The sidewalk will be on either side of the road;
- The pedestrians will either be on the sidewalk or the road;
- The remainder of the environment surrounds the road.

Taking this domain knowledge into account, Table 2 introduces the *reduced*, *wroadagents* and *wroadagents\_nodrivable* ordinal segmentation mask setups, including the ordinal relationship between classes in the form of a tree. Figure 5(b) shows the *reduced* ordinal segmentation mask setup for the autonomous driving scene in Figure 5(a).

## 4.2 Experimental Setup

The experimental results were obtained using the UNet architecture [20] with four groups of convolution blocks (each consisting of two convolution and one pooling



Figure 5: (a) Driving scene from the BDD100K dataset [18]. (b) Respective *reduced* mask.

Table 2: Segmentation classes. When using mask *reduced*, the classes in **gray** are replaced by a single class “road agents” which is equal to their union. Mask *wroadagents* uses all of the shown classes, while mask *wroadagents\_nodrivable* does not use the drivable area task classes in **blue**.

Index	Name	Semantic Segmentation	Drivable Area
1	unknown	unknown	–
└─ 2	environment	remaining	–
└─ 3	road	road	–
└─ 4	sidewalk	sidewalk	–
└─ 5	person	person	–
└─ 6	rider	rider	–
└─ 7	motorcycle	motorcycle	–
└─ 8	bicycle	bicycle	–
└─ 9	car	car	–
└─ 10	truck	truck	–
└─ 11	bus	bus	–
└─ 12	train	train	–
└─ 13	drivable area	–	alternative
└─ 14	ego lane	–	direct

layers) for each of the encoder and decoder portions<sup>1</sup>. All datasets were normalized with a mean of 0 and a standard deviation of 1 after data augmentation, consisting of random rotation, random horizontal flips, random crops, and random brightness and contrast. The networks were optimized for a maximum of 200 epochs in the case of the biomedical datasets and a maximum of 100 epochs in the case of the autonomous driving datasets, using the Adam [21] optimizer with a learning rate of 1e-4 and a batch-size of 16. Early stopping was used with a patience of 15 epochs. After a train-test split of 80-20%, a 5-fold training strategy consisting of 4 training folds and one validation fold was applied for each training dataset. For each fold, the best-performing model on the validation dataset was selected. An NVIDIA Tensor Core A100 GPU with 40GB of RAM and an NVIDIA RTX A2000 with 12GB of RAM were used to train the networks.

The metrics used were: (1) the Dice coefficient, which evaluates the methods with respect to the ground truth labels, (2) the contact surface, which evaluates the methods with respect to the spatial ordinal consistency, and (3) the percentage of unimodal pixels metrics, which evaluates the methods with respect to the pixel-wise ordinal consistency.

The cross-entropy loss and the methods by Fernandes et al. [5] were used as the baseline models. The methods to be evaluated had their parameterization, including the range of regularization term weights ( $\lambda$ ),

<sup>1</sup>An open-source PyTorch implementation of the UNet architecture was used, <https://github.com/milesial/Pytorch-UNet>.

empirically determined. These methods are:

- The semantic segmentation adaptation of the ordinal representation consistency  $L_{CO2}$  loss function, with the imposed margin  $\delta = 0.05$ , as recommended by the authors [3];
- The proposed ordinal structural loss for segmentation,  $L_{CSNP}$  and  $L_{CSDT}$ , with the distance transform threshold  $\delta = 0.5$  and the maximum regularization distance  $\gamma = 10$ ;
- The mix of representation and structural methods, through the  $L_{CO2} + L_{CSNP}$  loss combination of the two regularization terms.

## 5 Results

Tables 3–5 depict the main results. Since each loss term proposed is actually a penalty that is weighted with cross-entropy (loss = CE +  $\lambda$  term), each loss was evaluated using grid-search,  $\lambda \in \{0.1, 1, \dots, 10^4\}$ , selecting the best value for each metric.

Table 3 shows that the proposed losses generally offer an improvement, as judged by the Dice coefficient. Notice that this metric is computed for each pixel, explaining why CO2 (a loss that focuses on the pixel-wise ordinal representation consistency) generally performs better. Two additional tables are presented with the proposed ordinal metrics, evaluating the consistency for the representation space (% unimodality in Table 4) and the structural space (contact surface in Table 5). Naturally, CO2 again shows a very good performance for representation consistency, but the other losses start to become competitive as the structural consistency is evaluated using the contact surface metric.

Additional results are shown in plots that depict the influence of the weight of the regularization term,  $\lambda$ , on each respective metric. Figures 7, 8 and 9 show, respectively, the Dice coefficient, contact surface, and unimodal metrics for the biomedical datasets. We can see that the ordinal methods successfully optimize the ordinal metrics, resulting in more ordinally consistent models. The dice coefficient metric does not improve much; however, excessive regularization can occur at some  $\lambda$  values, resulting in a lower Dice metric.

Figure 10 shows the Dice coefficient for the autonomous driving datasets, including the out-of-distribution domain testing. There, it can be seen that CO2 is the method with the highest impact on the generalization capability of the model, achieving a maximum absolute gain of 4.2% (11.5% in relative terms) at  $\lambda = 10$ , which means that using this loss helps the model generalize better to previously unseen scenarios. Figure 11 showcases a set of model inference outputs for this scenario, comparing cross-entropy outputs to CO2 with  $\lambda = 10$ .

To evaluate whether the inclusion of domain knowledge during the training of the models would help the network learn better with scarce data for autonomous

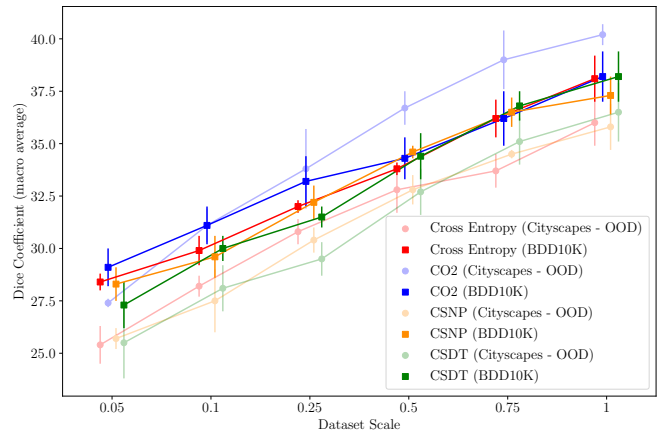


Figure 6: Dice coefficient (macro average) results for the autonomous driving datasets scale variation experiments (higher is better).

driving scenarios, an experiment that consisted of varying the scale of the dataset used to train the models was performed. For each method, the best-performing lambda in the out-of-distribution scenario was selected, the rationale being that those models are the best at generalizing to unseen scenarios, which is useful when training with low amounts of data. For the  $L_{CO2}$  and  $L_{CSNP}$  losses,  $\lambda = 10.0$  was used, and for the  $L_{CSDT}$ ,  $\lambda = 0.1$  was used. Figure 6 shows the Dice coefficient results for the dataset scale variation experiment.

When testing with the BDD10K dataset, the  $L_{CO2}$  and  $L_{CSNP}$  losses achieve better Dice coefficient results at scales 0.25 and 0.5 when compared with the cross-entropy baseline, which suggests that, indeed, these losses help the network learn better when data is scarce. Especially when using the CO2 loss, resulting in absolute gains of 1.2% (5.7% in relative terms) in the Dice coefficient performance at scale 0.25 over cross-entropy. CO2 continues beating cross-entropy Dice performance through scales 0.1 and 0.05.

Cross-entropy generalizes better than the spatial methods when testing with the Cityscapes dataset in an out-of-distribution scenario for lower scales. However, the CO2 loss continues to generalize better than the cross-entropy throughout all scales, achieving a maximum absolute gain of 5.3% (15.7% in relative terms) in the Dice coefficient at scale 0.75. Still, it can be seen that the generalization ability of CO2 decreases at a higher rate than its performance on BDD10K – training with fewer data has a higher impact on the model’s generalization ability.

Regarding the ordinal metrics, the scale variance does not significantly affect either metric.

In terms of compute complexity, since these are different losses, they do not affect inference time. Furthermore, any change in training time was too small to be detected.

### 5.1 Discussion

A comparison between the biomedical and autonomous driving datasets results concludes that the biomedical

Table 3: Overall results for the Dice coefficient metric.

Dataset	CrossEntropy	CO2	CSNP	CSDT	CO2+CSNP
Breast Aesthetics	93.8 ± 0.4	<b>94.2 ± 0.5</b>	94.0 ± 0.4	94.0 ± 0.5	94.0 ± 0.2
Cervix-MobileODT	77.0 ± 0.6	77.3 ± 0.7	<b>77.4 ± 0.2</b>	76.9 ± 0.7	77.3 ± 0.7
Mobbio	93.8 ± 0.1	<b>94.1 ± 0.0</b>	93.8 ± 0.0	93.7 ± 0.1	93.8 ± 0.1
Teeth-ISBI	74.0 ± 1.2	74.8 ± 0.4	74.9 ± 1.1	<b>75.3 ± 1.0</b>	74.7 ± 1.0
Teeth-UCV	90.2 ± 0.4	<b>90.8 ± 0.3</b>	90.5 ± 0.6	90.3 ± 0.3	90.5 ± 0.3
BDDIntersected reduced	71.2 ± 0.5	<b>71.9 ± 0.2</b>	71.2 ± 0.6	70.4 ± 0.6	<b>71.9 ± 0.2</b>
BDDIntersected noabstract	37.1 ± 0.8	<b>38.6 ± 0.8</b>	38.1 ± 0.5	37.2 ± 0.9	38.5 ± 0.9
BDD10K	38.1 ± 1.1	<b>39.2 ± 0.4</b>	38.2 ± 1.1	38.2 ± 1.2	<b>39.2 ± 0.4</b>
Cityscapes	36.0 ± 1.1	<b>40.2 ± 0.5</b>	35.8 ± 1.1	36.5 ± 1.4	39.3 ± 0.4

Table 4: Overall results for the percentage of unimodal pixels metric.

Dataset	CrossEntropy	CO2	CSNP	CSDT	CO2+CSNP
Breast Aesthetics	6.2 ± 0.5	<b>99.6 ± 0.2</b>	17.0 ± 16.0	13.2 ± 12.3	56.3 ± 7.4
Cervix-MobileODT	1.0 ± 0.2	<b>98.9 ± 0.4</b>	1.0 ± 0.2	0.9 ± 0.2	1.2 ± 0.2
Mobbio	0.8 ± 0.1	<b>97.3 ± 2.3</b>	0.9 ± 0.2	0.7 ± 0.2	0.9 ± 0.0
Teeth-ISBI	9.6 ± 3.2	<b>97.2 ± 0.2</b>	34.7 ± 12.3	38.1 ± 7.1	93.1 ± 1.4
Teeth-UCV	18.0 ± 1.6	<b>98.7 ± 0.2</b>	45.7 ± 9.0	34.7 ± 14.7	81.1 ± 13.0
BDDIntersected reduced	2.7 ± 1.7	<b>100.0 ± 0.0</b>	39.6 ± 18.0	55.1 ± 12.9	<b>100.0 ± 0.0</b>
BDDIntersected noabstract	2.4 ± 1.8	<b>100.0 ± 0.0</b>	46.0 ± 17.6	42.6 ± 7.1	<b>100.0 ± 0.0</b>
BDD10K	32.3 ± 5.8	<b>100.0 ± 0.0</b>	88.8 ± 2.4	96.4 ± 0.5	<b>100.0 ± 0.0</b>
Cityscapes	23.0 ± 11.4	<b>100.0 ± 0.0</b>	89.0 ± 5.2	97.2 ± 0.6	<b>100.0 ± 0.0</b>

Table 5: Overall results for the contact surface metric.

Dataset	CrossEntropy	CO2	CSNP	CSDT	CO2+CSNP
Breast Aesthetics	0.2 ± 0.2	<b>0.3 ± 0.1</b>	<b>0.3 ± 0.2</b>	<b>0.3 ± 0.2</b>	<b>0.3 ± 0.1</b>
Cervix-MobileODT	<b>14.5 ± 3.1</b>	<b>14.5 ± 2.4</b>	14.2 ± 1.8	13.6 ± 1.4	<b>14.5 ± 2.4</b>
Mobbio	12.3 ± 0.4	<b>12.5 ± 0.4</b>	12.3 ± 0.3	12.4 ± 0.5	12.0 ± 0.2
Teeth-ISBI	30.0 ± 3.5	<b>31.2 ± 2.6</b>	30.4 ± 1.7	29.1 ± 1.0	<b>31.2 ± 2.6</b>
Teeth-UCV	7.0 ± 1.1	6.9 ± 1.1	<b>8.1 ± 1.3</b>	5.5 ± 0.9	6.9 ± 1.1
BDDIntersected reduced	55.9 ± 3.5	54.9 ± 2.5	<b>56.4 ± 1.4</b>	54.5 ± 3.2	52.8 ± 2.6
BDDIntersected noabstract	47.8 ± 2.2	<b>50.1 ± 2.2</b>	49.9 ± 1.8	47.0 ± 1.1	48.5 ± 1.5
BDD10K	<b>51.2 ± 2.1</b>	50.5 ± 2.5	50.3 ± 1.2	50.9 ± 1.4	48.7 ± 2.1
Cityscapes	59.3 ± 2.0	<b>61.4 ± 1.4</b>	58.0 ± 2.1	60.2 ± 2.5	57.6 ± 3.9



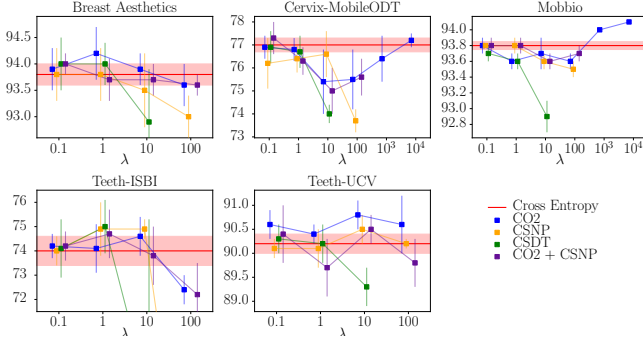


Figure 7: Dice coefficient (macro average) results for the biomedical datasets (higher is better).

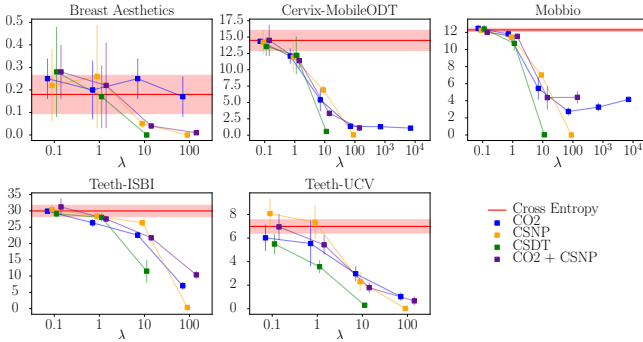


Figure 8: Contact surface results for the biomedical datasets (lower is better).

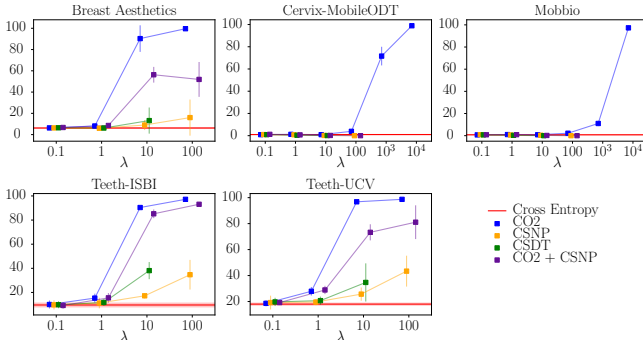


Figure 9: Percentage of unimodal pixels results for the biomedical datasets (higher is better).

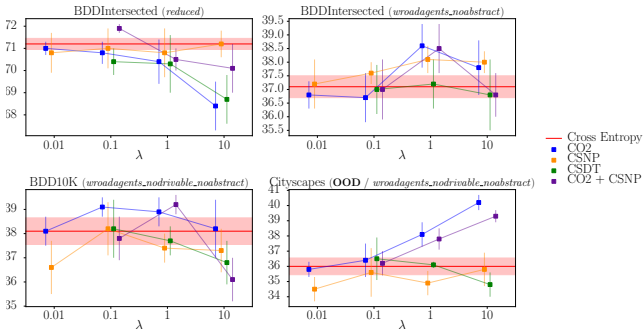
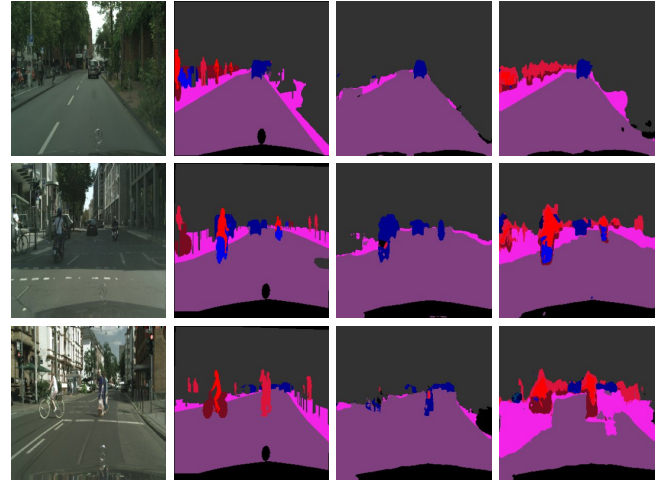


Figure 10: Dice coefficient (macro average) results for the autonomous driving datasets (higher is better).



(a) (b) (c) (d)

Figure 11: Comparison of the influence of cross-entropy and CO2 losses on model output in out-of-distribution inference. (a) Input image. (b) Ground-truth. (c) Cross-entropy. (d) CO2 ( $\lambda = 10.0$ ). The CO2 loss promotes more accurately identification of pedestrians, two-wheel vehicles, and riders when compared with the cross-entropy loss output.

results are significantly better in terms of the Dice coefficient performance – the performance gains with the autonomous driving datasets are still positive, but not as large, since these datasets are considerably more complex, with a greater variety of scenarios and segmentation classes.

The representation space, i.e., pixel-wise,  $L_{CO2}$  performed well in both the biomedical and autonomous driving datasets, especially when considered in an out-of-distribution domain – it could potentially be applied in a real-world scenario in order to improve the generalization capabilities of perception algorithms.

The structured space, i.e., spatial,  $L_{CSNP}$  and  $L_{CSDT}$  losses, may not apply to the autonomous driving scenario in their current form, at least at high regularization weights. The scene perspective from the car makes it so that there is a large amount of valid contact surface between non-ordinally adjacent classes – in a 2D projection of the real world, the absolute minimization of these contact surfaces may not be the best solution since occlusions and different perspectives may originate legitimate contact between non-ordinally adjacent classes. Relaxed adaptations of these methods that consider this type of contact could be devised in the future. However, in the biomedical datasets, these methods performed well, with their greatest difficulty being the existence of occlusions.

As seen, the choice of  $\lambda$  value, i.e., regularization weight, is critical for the performance of the proposed methods. For this reason, in order to be applied to different domains, there should be an empirical study of the influence of the lambda value in the segmentation performance in that specific domain and the choice of a value that is a balance between the ordinal metrics and the Dice coefficient, i.e., a value that promotes some

unimodality and spatial consistency but also does not hurt Dice performance to the point where it is unusable.

## 6 Conclusion

This paper explored ordinality in the context of structured data, proposing a formal definition of an ordinal model for generic graph structures. The concept was then specifically studied for semantic segmentation, where each image can be interpreted as a graph.

In this domain, two categories of loss functions for ordinal segmentation were studied: (1) an ordinal representation consistency loss, where each pixel is treated individually by promoting unimodality in its probability distribution, and (2) a structural consistency loss, where each pixel is considered in the context of its neighborhood and the contact surface between non-ordinally adjacent classes is minimized.

For that purpose, the following loss terms were proposed:

1. the segmentation adaptation of the representation  $L_{CO2}$  loss;
2. the structural  $L_{CSNP}$  loss, which considers only the immediate neighbor pixels;
3. the structural  $L_{CSDT}$  loss, which considers the global neighborhood.

In addition, two metrics were proposed to evaluate the network output’s ordinal consistency: (1) the percentage of unimodal pixels and (2) the contact surface between the segmentation masks of non-ordinally adjacent classes.

The proposed methods were initially validated on five biomedical datasets and two autonomous driving datasets, resulting in more ordinally consistent models without significantly impacting the Dice coefficient. To evaluate the methods’ impact on the models’ generalization capability, the resulting models were tested in an autonomous driving out-of-distribution scenario. Furthermore, the autonomous driving models were also tested with scaled-down versions of the BDD100K dataset to evaluate how the network learns with scarce data. The ordinal methods achieved maximum improvements in the Dice coefficient with an absolute value of 5.3% (15.7% in relative terms) in the out-of-distribution domain.

To summarize, incorporating ordinal consistency into semantic segmentation models showed promising results, including developing more generalizable models that exhibit improved learning capabilities with limited data availability. Since these are loss terms, they do not add time complexity to inference time.

Future research topics could include: (i) the development of more flexible spatial ordinal segmentation methods, allowing for limited contact between non-ordinally adjacent classes, such as in the case of occlusions and different perspectives; and (ii) the develop-

ment of novel methods that leverage ordinal constraints not necessarily consisting of augmented loss functions.

Furthermore, the current work could contribute to other types of consistency. The partially ordered domains explored in this work were structural (e.g., a vehicle may be located on the road or in parking spaces), but a representational partially ordered domain could correspond to hierarchical segmentation [22], where each pixel has a taxonomy (e.g., a motorcycle and bicycle are both two-wheels; two-wheels and four-wheels are both types of vehicles).

Also, part segmentation could be considered a different type of structural consistency, where parts of an object are next to each other. Super-pixels have been used to impose constraints, such as the “head” appearing above “upper body” or “hair” being above “head” [23]. Similarly, the function of Restricted Boltzmann Machines has been used to favor certain classes based on their spatial locations [24]. This work could be considered an alternative that promotes such structural consistency using loss penalties.

## 7 Source Code

```
def CSNP(P, K):
    loss = 0
    count = 0

    # for each pair of non-ordinally adjacent classes
    for k1 in range(K):
        for k2 in range(K):
            if abs(k2 - k1) <= 1:
                continue

            # more weight to more ordinally distant classes
            ordinal_multiplier = abs(k2 - k1) - 1

            dx = P[:, k1, :, :-1] * P[:, k2, :, 1:]
            dy = P[:, k1, :-1, :] * P[:, k2, 1:, :]

            loss += ordinal_multiplier * \
                (torch.mean(dx) + torch.mean(dy))/2
            count += 1

    if count != 0:
        loss /= count
    return loss

def CSDT(P, K, threshold=.5, max_dist=10.):
    loss = 0
    count = 0

    activations = 1. * (P > threshold)
    DT = distance_transform(activations)

    # cap the maximum distance at 10
    max_dist_DT = (DT >= max_dist) * max_dist
    # select the values with a distance < 10
    DT *= DT < max_dist
    # add the capped values
    DT += max_dist_DT

    # for each pair of non-ordinally adjacent classes
    for k1 in range(K):
        for k2 in range(k1 + 2, K):
            # more weight to more ordinally distant classes
            ordinal_multiplier = abs(k2 - k1) - 1

            d_k1, d_k2 = DT[:, k1], DT[:, k2]
            p_k1, p_k2 = P[:, k1], P[:, k2]

            calc = p_k1 * d_k2 + p_k2 * d_k1
            calc = calc[calc != 0]

            loss += ordinal_multiplier * torch.mean(calc)
            count += 1

    if count != 0:
```

```

loss /= count
loss /= max_dist # normalize
return -loss # maximize

```

## References

- [1] J. Tang, S. Li, and P. Liu, “A review of lane detection methods based on deep learning,” *Pattern Recognition*, vol. 111, p. 107623, Mar. 2021. [Online]. Available: <https://www.sciencedirect.com/science/article/pii/S003132032030426X>
- [2] R. Cruz, K. Fernandes, J. F. Pinto Costa, M. P. Ortiz, and J. S. Cardoso, “Ordinal class imbalance with ranking,” in *Pattern Recognition and Image Analysis: 8th Iberian Conference, IbPRIA 2017, Faro, Portugal, June 20-23, 2017, Proceedings 8*. Springer, 2017, pp. 3–12.
- [3] T. Albuquerque, R. Cruz, and J. S. Cardoso, “Ordinal losses for classification of cervical cancer risk,” *PeerJ Computer Science*, vol. 7, p. e457, Apr. 2021, publisher: PeerJ Inc. [Online]. Available: <https://peerj.com/articles/cs-457>
- [4] —, “Quasi-unimodal distributions for ordinal classification,” *Mathematics*, vol. 10, no. 6, p. 980, 2022.
- [5] K. Fernandes and J. S. Cardoso, “Ordinal Image Segmentation using Deep Neural Networks,” in *2018 International Joint Conference on Neural Networks (IJCNN)*, Jul. 2018, pp. 1–7, iSSN: 2161-4407.
- [6] J. F. Pinto da Costa, H. Alonso, and J. S. Cardoso, “The unimodal model for the classification of ordinal data,” *Neural Networks*, vol. 21, no. 1, pp. 78–91, Jan. 2008. [Online]. Available: <https://www.sciencedirect.com/science/article/pii/S089360800700202X>
- [7] C. Beckham and C. Pal, “Unimodal probability distributions for deep ordinal classification,” Jun. 2017, arXiv:1705.05278 [stat]. [Online]. Available: <http://arxiv.org/abs/1705.05278>
- [8] J. S. Cardoso, R. Cruz, and T. Albuquerque, “Unimodal Distributions for Ordinal Regression,” Mar. 2023, arXiv:2303.04547 [cs]. [Online]. Available: <http://arxiv.org/abs/2303.04547>
- [9] J. Cheng, “A neural network approach to ordinal regression,” Apr. 2007, arXiv:0704.1028 [cs]. [Online]. Available: <http://arxiv.org/abs/0704.1028>
- [10] J. S. Cardoso and R. Sousa, “Classification models with global constraints for ordinal data,” in *2010 Ninth International Conference on Machine Learning and Applications*. IEEE, 2010, pp. 71–77.
- [11] R. Sousa and J. S. Cardoso, “Ensemble of decision trees with global constraints for ordinal classification,” in *2011 11th International Conference on Intelligent Systems Design and Applications*. IEEE, 2011, pp. 1164–1169.
- [12] T. Strutz, “The distance transform and its computation,” *arXiv preprint arXiv:2106.03503*, 2021.
- [13] J. S. Cardoso and M. J. Cardoso, “Towards an intelligent medical system for the aesthetic evaluation of breast cancer conservative treatment,” *Artificial Intelligence in Medicine*, vol. 40, no. 2, pp. 115–126, Jun. 2007. [Online]. Available: <https://www.sciencedirect.com/science/article/pii/S0933365707000206>
- [14] Intel, “Intel & MobileODT Cervical Cancer Screening,” <https://kaggle.com/competitions/intel-mobileodt-cervical-cancer-screening>, accessed: 2023-06-22. [Online]. Available: <https://kaggle.com/competitions/intel-mobileodt-cervical-cancer-screening>
- [15] A. F. Sequeira, J. C. Monteiro, A. Rebelo, and H. P. Oliveira, “MobBIO: A multimodal database captured with a portable handheld device,” in *2014 International Conference on Computer Vision Theory and Applications (VISAPP)*, vol. 3, Jan. 2014, pp. 133–139.
- [16] C.-W. Wang, C.-T. Huang, J.-H. Lee, C.-H. Li, S.-W. Chang, M.-J. Siao, T.-M. Lai, B. Ibragimov, T. Vrtovec, O. Ronneberger, P. Fischer, T. F. Cootes, and C. Lindner, “A benchmark for comparison of dental radiography analysis algorithms,” *Medical Image Analysis*, vol. 31, pp. 63–76, Jul. 2016. [Online]. Available: <https://www.sciencedirect.com/science/article/pii/S1361841516000190>
- [17] K. Fernandez and C. Chang, “Teeth/Palate and Interdental Segmentation Using Artificial Neural Networks,” in *Artificial Neural Networks in Pattern Recognition*, ser. Lecture Notes in Computer Science, N. Mana, F. Schwenker, and E. Trentin, Eds. Berlin, Heidelberg: Springer, 2012, pp. 175–185.
- [18] F. Yu, H. Chen, X. Wang, W. Xian, Y. Chen, F. Liu, V. Madhavan, and T. Darrell, “BDD100K: A diverse driving dataset for heterogeneous multitask learning,” in *IEEE/CVF Conference on Computer Vision and Pattern Recognition (CVPR)*, June 2020.
- [19] M. Cordts, M. Omran, S. Ramos, T. Rehfeld, M. Enzweiler, R. Benenson, U. Franke, S. Roth, and B. Schiele, “The Cityscapes Dataset for Semantic Urban Scene Understanding,” Apr. 2016, arXiv:1604.01685 [cs]. [Online]. Available: <http://arxiv.org/abs/1604.01685>

- [20] O. Ronneberger, P. Fischer, and T. Brox, “U-Net: Convolutional Networks for Biomedical Image Segmentation,” May 2015, arXiv:1505.04597 [cs] version: 1. [Online]. Available: <http://arxiv.org/abs/1505.04597>
- [21] D. P. Kingma and J. Ba, “Adam: A Method for Stochastic Optimization,” Jan. 2017, arXiv:1412.6980 [cs]. [Online]. Available: <http://arxiv.org/abs/1412.6980>
- [22] L. Li, T. Zhou, W. Wang, J. Li, and Y. Yang, “Deep hierarchical semantic segmentation,” in *Proceedings of the IEEE/CVF Conference on Computer Vision and Pattern Recognition*, 2022, pp. 1246–1257.
- [23] Y. Bo and C. C. Fowlkes, “Shape-based pedestrian parsing,” in *CVPR 2011*. IEEE, 2011, pp. 2265–2272.
- [24] S. Tsogkas, I. Kokkinos, G. Papandreou, and A. Vedaldi, “Deep learning for semantic part segmentation with high-level guidance,” *arXiv preprint arXiv:1505.02438*, 2015.